

# Properties of 50–110-GHz Waveguide Components Fabricated by Metal Additive Manufacturing

Shane Verploegh<sup>1</sup>, *Member, IEEE*, Mike Coffey, *Member, IEEE*, Erich Grossman, *Senior Member, IEEE*, and Zoya Popović, *Fellow, IEEE*

**Abstract**—This paper presents several V-band (50–75 GHz) WR-15 and W-band (75–110 GHz) WR-10 waveguide components fabricated using both direct metal laser sintering in aluminum, nickel-chromium, maraging steel (MS), and copper alloys and stereolithography in copper-coated plastic. Printing resolution is analyzed with respect to feature creation. The RF performance and surface roughness are measured, and the loss due to surface roughness quantified. The measured loss for WR-10 at 92.5-GHz ranges from 5.5 dB/m for the copper-plated plastic waveguides to 36.9 dB/m for the nickel alloy and for WR-15 at 62.5-GHz ranges from 11.0 dB/m for the aluminum alloy to 14.4 dB/m for the MS alloy. From a loss budget study, it is found that standard models do not accurately predict loss due to surface roughness for rough surfaces where the height variation is much larger than skin depth  $\delta$ . It is also found that for internally complex printing, the MS alloy versions maintain the closest structure to designed components and expected RF performance. This paper presents the current state-of-the-art in available additive-manufactured waveguide components at V- and W-bands.

**Index Terms**—Additive manufacturing (AM), direct metal laser sintering (DMLS), surface roughness, 3-D printing, V-band, waveguides, W-band.

## I. INTRODUCTION

**M**OTIVATION for the recent interest in additive manufacturing (AM) for microwave and millimeter-wave components is the potential for reduced cost and weight, shorter fabrication times and the ability to fabricate assembly geometries not possible with traditional split-block machining techniques [1]. AM is especially attractive for higher frequency metallic waveguide components, and there are a limited number of technologies that can provide conductor printing, most of them with roughness that is considered to be too high for low loss at frequencies above V-band. Published results include a variety of passive components over a wide range of frequencies with different fabrication techniques.

Manuscript received July 1, 2017; revised September 6, 2017 and October 10, 2017; accepted October 12, 2017. Date of publication November 27, 2017; date of current version December 12, 2017. This work was supported by the Defense Advanced Research Projects Agency under Contract HR001-16-C-0085. This paper is an expanded version from the IEEE MTT-S International Microwave Symposium Conference, Honolulu, HI, USA, June 4–9, 2017. (*Corresponding author: Shane Verploegh.*)

S. Verploegh, M. Coffey, and Z. Popović are with the Department of Electrical, Computer, and Energy Engineering, University of Colorado Boulder, Boulder, CO 80309 USA (e-mail: shane.verploegh@colorado.edu).

E. Grossman is with the Physical Measurement Laboratory, National Institute of Standards and Technology, Boulder, CO 80305 USA.

Color versions of one or more of the figures in this paper are available online at <http://ieeexplore.ieee.org>.

Digital Object Identifier 10.1109/TMTT.2017.2771446

A majority of work to date demonstrates plated plastic waveguide components using stereolithography (SLA) and fused deposition modeling (FDM). For example, additive manufactured copper-coated SLA waveguides at 10.7–12 GHz replace an antenna feed chain with no signal degradation observed [2]. A lightweight  $2 \times 2$  horn antenna array with a complex feeding network is designed and fabricated for Ka-band using electroless copper-plated SLA [3]. Split block W-band through lines and 6th-order iris bandpass filters printed using plated FDM and SLA are demonstrated in [4]. The through lines demonstrate attenuation of 11 dB/m at the band edges, while an unloaded quality factor of 152 is measured [4]. This paper also gives a good comparison with existing waveguide components. Groove gap waveguide at Ka-band is printed in metalized SLA with average measured losses of 1.4 dB/m [5]. Termination structures at X-band are characterized in [6], where the printed part is inserted into through lines. Single-block W-band bandpass filters are designed and fabricated using laser micromachining and copper-plated SLA with good agreement between simulated and measured results [7]. While metal-coated plastic waveguides can be rapidly prototyped and are smooth, they tend to be fragile and the fabrication processes are not commercially available.

Alternatively, direct printing with metal powders can be used: selective laser melting (SLM), selective laser sintering (SLS), and direct metal laser sintering (DMLS). For example, bandpass filters for E-band are fabricated using SLM with Cu–15Sn alloy powder, and a shifted passband and increased insertion loss are observed [8]. Using SLM with Cu–15Sn alloy powder, rectangular through lines are fabricated at E-, D-, and H-bands, with average E-band attenuation of 7.51 and 7.76 dB/m for 50- and 100-mm waveguide lengths, respectively [9].

In [10], performance of W-band dominant-mode metal waveguide sections fabricated with several AM techniques is presented. The focus of this paper presented here is to evaluate various commercially-available metal AM fabrication techniques for both V-band (WR-15) and W-band (WR-10) waveguide components in terms of loss due to material properties and surface roughness, as well as effects of feature size printing limitations. Using DMLS in various aluminum and nickel alloys, as well as copper and maraging steel (MS), we present results of two simple components, a 10-cm straight waveguide section and a 20-dB directional coupler, as shown in Figs. 1 and 2, respectively. Comparison for



Fig. 1. Photograph of straight 10-cm WR-10 waveguides implemented in a variety of materials. From left to right: MCP, GRCoP-84 (Cu), Inconel 625 (Ni), 3 AlSi10Mg with different laser settings, and MS.



Fig. 2. Photograph of WR-10 20-dB waveguide couplers implemented in a variety of materials. From left to right: MCP, 3 AlSi10Mg with different laser settings, and MS.

a more functionally complex component is also discussed for the case of a filter made with a row of symmetrical small corrugations, testing the feature resolution effect on performance. Measured  $S$ -parameters are used to study the loss due to material conductivity, dimension-introduced mismatch, and surface roughness. The surface finish of the waveguide components is measured and quantified using focus-variation microscopy (FVM) using a digital microscope (Keyence VHX 1000E) and the results are analyzed and compared to existing models for loss due to surface roughness.

This paper is outlined as follows. Section II describes component design and overviews the various manufacturing methods, related material properties, and spatial resolution limitations. Section III presents measured small-signal broadband  $S$ -parameters and compares the performance. Section IV discusses surface roughness measurements and quantifies increase in loss due to surface roughness. In Section V, an analysis of the measured data reveals issues with common roughness modeling techniques. In the last section, recommendations for DMLS are made in relation to material choice and feature printing.

## II. WAVEGUIDE COMPONENT DESIGN, MANUFACTURING, AND FEATURE RESOLUTION

The waveguide components are designed using finite-element modeling (HFSS) with measured conductivity data assuming smooth walls and fabricated with a variety of materials and printing methods, described below. A limitation

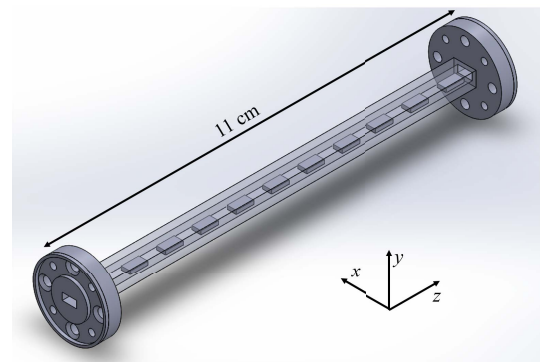


Fig. 3. 3-D view of WR-10 filter waveguide section with a transparent midsection. The filter is comprised of 11 blocks of the same width, height, and depth in a WR-10 straight waveguide section. A similar filter was designed for V-band in WR-15 waveguide.

of standard split-block machining that becomes an issue at millimeter wavelengths is the radius of curvature due to bit size. In the case of AM, the limitation will be due to machine tolerance and alloy properties, described in Section II-B.

### A. Component Design and Construction

The 10-cm straight 20-dB coupler and filter W-band waveguide components, shown in Figs. 1–3, are designed as single pieces in Ansoft HFSS and use standard UG-387 for WR-10 (MIL-DTL-3922/67E) flanges. In addition, 11-cm straight, 20-dB coupler, and filter V-band waveguide components are designed in Ansoft HFSS and use UG-385 for WR-15 (MIL-DTL-3922/67E) flanges; these V-band parts are only printed in two DMLS alloys, AlSi10Mg (aluminum) and MS1 (MS). Some of the components include an "anti-cocking" ring around the edge of the flanges. This outer flange ring helps prevent misalignment due to part angle and varied screw tightness during testing.

Various metallic alloys in powder form are available for DMLS; in this paper we use AlSi10Mg, an aluminum alloy; GRCoP-84, a copper alloy referred to as Cu; MS1, maraging steel referred to as MS; and Inconel 625, nickel-chromium superalloy referred to as Ni. These parts were printed on Electro Optical Systems (EOS) DMLS machines EOSINT M270/M280 and EOS M290 through manufacturing suppliers Midwest Composite and Visser Precision, respectively. The SLA components were plated in copper using a proprietary electroless process via supplier Swissto12; these parts are referred to as metal (Cu) coated plastic (MCP).

Conventional 4-point probe resistivity testing was performed on both MS1 and AlSi10Mg parts. The measured conductivity for MS1 is found to be  $1.60 \times 10^6$  S/m; the measured conductivity for AlSi10Mg is found to be  $2.66 \times 10^7$  S/m. A summary of the material properties and referred names are shown in Table I.

The DMLS process uses 20–40- $\mu$ m metal particles that are sintered together with a Yb-fiber laser with a focused finite spot diameter that varies in both size and intensity with output power. Table II lists the machine standard settings (laser power, focus diameter, and scan speed) employed by different manufacturers. Since waveguide features at

TABLE I  
METAL POWDER ALLOY PROPERTIES

Alloy	Referred Name	Bulk $\sigma$ (S/m)	Measured $\sigma$ (S/m)
MS1*	MS	$2.05 \times 10^6$	$1.60 \times 10^6$
AlSi10Mg**	A1, A2, A3	$1.8\text{-}2.5 \times 10^7$	$2.66 \times 10^7$
Inconel 625***	Ni	$7.75 \times 10^5$	-
GrCop-84****	Cu	$4.17 \times 10^7$	-

\* For more information on MS1 see EOS material list.

\*\* For more information on AlSi10Mg see EOS material list and [11].

\*\*\* For more information on Inconel 625 see EOS material list.

\*\*\*\* Taken at room temperature. For more information on GrCop-84 see [12].

TABLE II  
DMLS PROCESSING PARAMETERS

	Machine	Power (W)	Focus ( $\mu\text{m}$ )	Scan Speed (mm/s)
MC	M270/280	200 or 400	100	750
VP	M290	400	100	500-850

millimeter-wave frequencies are usually smaller than  $100 \mu\text{m}$ , different laser scanning strategies are employed. Typically, laser output power, spot speed, and distance between multiple sintered lines, hatches, are varied.

During the sintering process, the direction of the component build fundamentally changes the spatial resolution of internal features and measured surface roughness. For clarity in the build direction, as denoted in Fig. 3, the  $xy$ -plane is defined as the machine bed and powder is layered upward in the  $z$ -direction. In the straight sections, the build direction is straight upward ( $z$ -direction) from the build plate with the flanges parallel to the build plate ( $xy$ -plane) of the DMLS machine. For the internally complex components, the 20-dB couplers and the filters, there are always a few walls with no structural support during build. This lack of support causes the melt pool to bend downward into untouched powder space. In order to minimize this bend, the component is tilted in the  $xz$ -plane by  $45^\circ$ . The part is still built along the  $z$ -direction.

In this paper, three WR-10 AlSi10Mg straight components (A1, A2, and A3) are printed as can be seen in Fig. 1. A1 (Midwest Composite) and A2 (Visser Precision) are printed using the standard manufacturer settings seen in Table II. A3 (Visser Precision) is printed with higher energy density in the perimeter scan. In using a higher energy density, less surface roughness occurs, however, the component has reduced feature resolution. This is discussed in more detail in Section II-B.

The simulated WR-10 20-dB coupler design uses 12 identical round coupling holes in a periodic array. The resolution of the DMLS process allows for a minimum wall thickness of  $0.3 \text{ mm}$  and a minimum feature size of  $120 \mu\text{m}$ . The WR-10 20-dB coupler DMLS design utilized a  $0.508\text{-mm}$  hole diameter and a horizontal (defined here as “along-guide,” vertical being “across-guide”) center-to-center hole spacing of  $1.375 \text{ mm}$ . Fig. 4(a) shows the fabricated dimensions of the WR-10 component. Because of the SLA process limitations, a second WR-10 coupler was designed with a larger hole spacing at the expense of bandwidth.

The WR-15 20-dB coupler design uses 14 identical round coupling holes in a periodic array. The DMLS fabricated

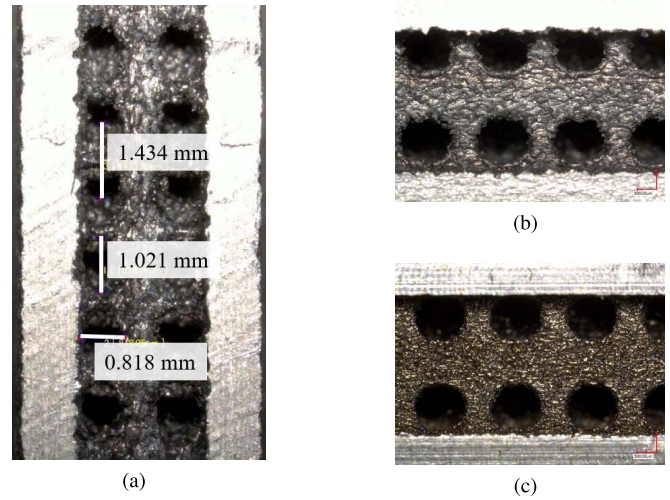


Fig. 4. Photographs of the interior coupling holes of 20-dB directional couplers after destructive testing. (a) WR-10 A1 component with measured dimensions. (b) WR-15 AlSi10Mg component. (c) WR-15 MS component. Measured dimensions for (b) and (c) are discussed in Section II-B, Fig. 5, and Table II. The images are created using FVM at  $\times 50$  magnification.

WR-15 20-dB coupler design utilizes a  $0.62\text{-mm}$  hole diameter and a horizontal center-to-center hole spacing of  $1.99 \text{ mm}$  and a vertical center-to-center hole spacing of  $2.33 \text{ mm}$ . Fig. 4(b) and (c) illustrate the dramatic printing improvement with WR-15’s larger dimensions.

The symmetrical filter design uses 11 blocks with consistent height, width, and depth for both WR-10 and WR-15. Tolerance issues with the DMLS process were taken into account during the design process. Fig. 3 shows this design for WR-10 clearly. Both WR-15 and WR-10 waveguide filter designs were created in AlSi10Mg and MS1.

### B. Feature Resolution Analysis

Precise feature printing becomes a critical issue in the construction of functionally more complex components. Here we characterize the complex internals of the WR-15 waveguide components and the apertures of the WR-10 waveguide components in relation to designed specifications.

In DMLS, the internal coupling holes are created using a varied hatch pattern per deposition layer due to the lack of support at the hole edges and suspension between guides. During the cooling of the melt pool at each layer, the edges of the coupling holes harden with a roughness difficult to predict. The edge roughness is quantified by the root mean square deviation (RMSD) from the designed hole to the printed one. In addition to finding the hole RMSD, the horizontal and vertical center-to-center hole spacing is determined and compared to specification.

Using FVM images at magnitudes of 100 and 50 and a generalized Hough Transform on a Canny-filtered image with techniques developed in [13] and [14], the center point of a single hole can be found and then used to overlay a circle with the dimensions of the WR-15 coupler design. The original image is then segmented by using a fast marching method based on pixel weights derived from the image gradient; using

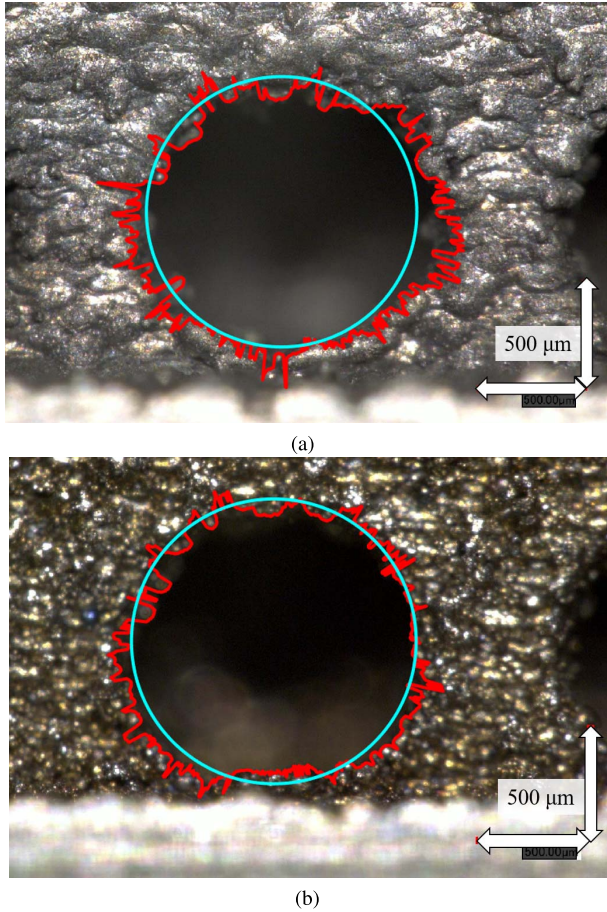


Fig. 5. WR-15 20-dB coupler holes images. (a) AlSi10Mg and (b) MS1 with superimposed lines for the designed hole specification and an algorithmically-found printed edge (jagged line). The images are created with FVM at  $\times 100$  magnification. The scale shown is  $500 \mu\text{m}$ .

TABLE III  
WR-15 COUPLER HOLE MISALIGNMENT

	RMSD ( $\mu\text{m}$ )	Avg. Horiz. (mm)	Avg. Vert. (mm)
AlSi10Mg	83.8	1.95	2.22
MS	50.2	1.94	2.31
Ideal	0	1.99	2.33

the center point, the algorithm radially sweeps the segmented image to find the coupling hole edge, overlaid on the original image as shown in Fig. 5. This analysis is also performed on the images shown in Fig. 4(b) and (c) for finding the center points of each hole. Using these points, the vertical and horizontal center-to-center hole spacing is determined.

A summary of WR-15 coupler hole misalignment with comparison to designed specifications is shown in Table III. The MS has better edge structure, as evidenced by RMSD, and is generally closer to designed center-to-center spacing than the AlSi10Mg component.

For the filter, the deviation between fabricated and simulated geometric features is essential for frequency response modeling. Fig. 6 shows fabricated dimensions; both components deviate from the designed structure. The MS is smaller in total

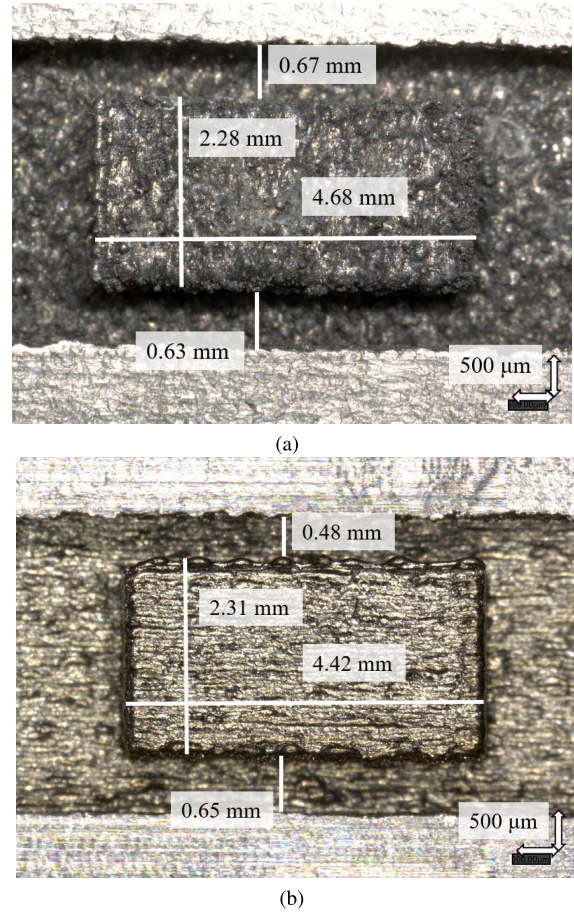


Fig. 6. WR-15 filter images centered on the raised blocks, taken with FVM at a magnitude of 50, with overlaid lines for measured distances. The scale shown is  $500 \mu\text{m}$ .

TABLE IV  
WR-15 FILTER CORRUGATION SIZE AND MISALIGNMENT

	Vert. (mm)	Horiz. (mm)	Avg. Wall Deviation ( $\mu\text{m}$ )
AlSi10Mg	2.28	4.68	29.6
MS	2.31	4.42	114.6
Ideal	2.4	4.63	0

area whereas the AlSi10Mg is slightly longer horizontally but smaller vertically than designed. The MS corrugation is shifted closer to one sidewall.

A summary of the WR-15 filter corrugation size and misalignment is shown in Table IV.

A feature issue that becomes more visually obvious at WR-10 proportions than WR-15 is misprinted aperture dimensions. Fig. 7 shows four FVM images of the WR-10 waveguide apertures in different materials. By standard designation, WR-10 aperture dimensions are  $2.54 \text{ mm} \times 1.27 \text{ mm}$ . However, the printed dimensions are as much as 13% and 34% larger in the  $x$ - and  $y$ -directions, respectively. For the GRCop-84 waveguide, Fig. 7(a), this creates an impedance mismatch to a standard flange which can be seen in return and insertion loss measurements. AlSi10Mg A3, Fig. 7(d), which is created using a higher energy density has a rounded shape. In RF

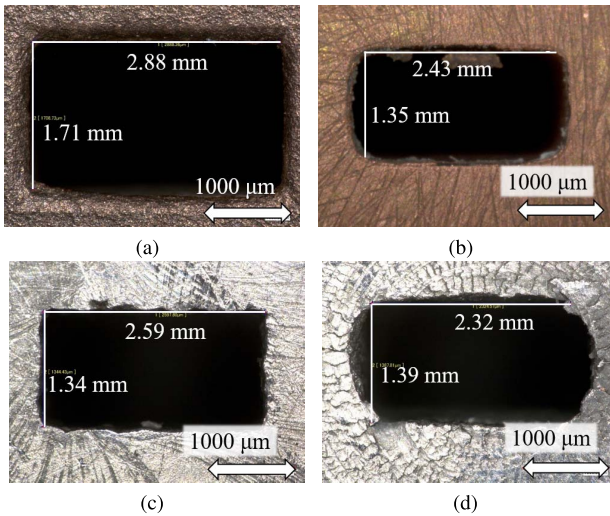


Fig. 7. WR-10 aperture dimension deviation for (a) Cu, (b) MCP, (c) AlSi10Mg A2, and (d) AlSi10Mg A3 waveguide section. WR-10 aperture dimension for designed components is 2.54 mm  $\times$  1.27 mm.

performance, this shape causes loss due to higher-order mode excitation at higher frequencies. The MCP and AlSi10Mg A2 components have the closest dimensions to the standard.

### III. MEASURED RF PERFORMANCE

RF performance is shown in this section for the waveguide components shown in Figs. 1–3 fabricated in different materials as discussed in Section II-A. The RF performance was measured with an HP8510C with W85104A W-band and V85104A V-band frequency extenders. Calibration was performed using calibration kits HP W11644A for WR-10 and V11644A for WR-15, resulting in  $|S_{11}| < -30$  dB for the termination standards.

The measured  $|S_{21}|$  parameters of the straight 10-cm WR-10 waveguide sections are shown in Fig. 8. While  $|S_{11}| < -10$  dB for nearly all WR-10 straight 10-cm components,  $|S_{21}|$  varies for each material and best performance across-band is observed with MCP. In reference to the aperture mismatch, A2 can be seen having a fairly flat response as the component was close to design. The Cu component has a consistently large standing wave across-band. Ni and Al have poor responses across the entire band.

For the WR-15 straight 11-cm waveguide sections in MS and aluminum, Fig. 9 shows  $|S_{21}|$  data. Using the measured conductance described in Section II-A, components in HFSS were simulated and are shown in Fig. 9 for a comparison between design and printed. While  $|S_{11}| < -20$  dB for both components,  $|S_{21}|$  varies for each material and a flat performance across-band is observed with MS.

With this specific production run, another printing problem was found in the AlSi10Mg. Thin stalactites, stalagmites, and threads of metal connecting walls are easily visible within the waveguide. This phenomenon is explained by liquid metal expulsion [15]. During lasering and due to differing pressures, a recoil force can exist on the melt pool causing liquid metal to be expelled onto cooled surfaces. In the first measurement

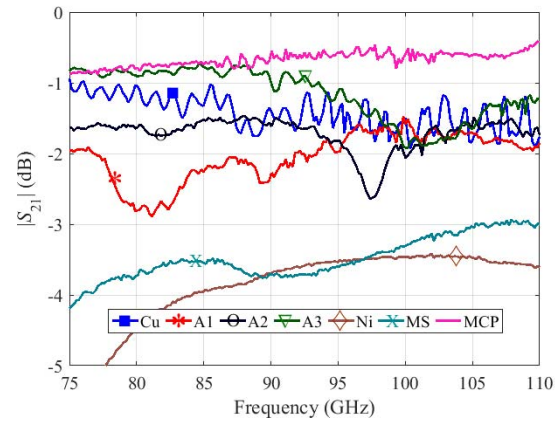


Fig. 8.  $|S_{21}|$  data for the various fabricated WR-10 10-cm waveguide sections. It is assumed the standing wave patterns or poor across-band response is due to aperture dimension deviation and/or imperfect flange mating.

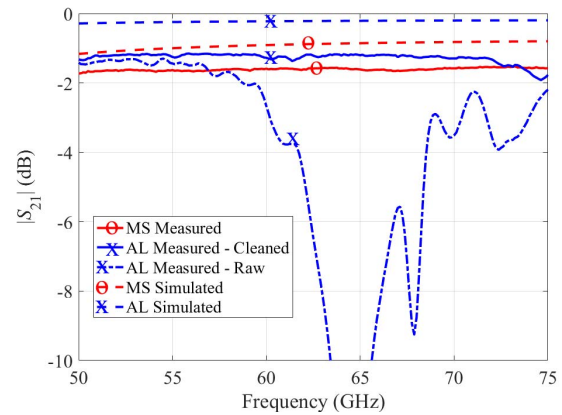


Fig. 9.  $|S_{21}|$  data for the fabricated WR-15 11-cm waveguide sections. The easily visible misprinted threads in the AlSi10Mg, as discussed in this section, are assumed to be causing significant amounts of reflections. The response improves after cleaning. The HFSS simulation data using the conductivity results of the four point probe measurements are included.

of this aluminum part, these "misprints" caused significant reflection loss at unexpected frequencies. After cleaning the AlSi10Mg waveguide section with a nonabrasive material (so that surface roughness was left intact) and subsequently flushing with acetone, the large drops in  $|S_{21}|$  are removed and a flatter response is seen.

A summary of the S-parameter data for both WR-10 and WR-15 straight components at center frequencies (92.5 GHz for W-band and 62.5 GHz for V-band) is given in Table V.

The S-parameters of the various WR-10 20-dB couplers are shown in Fig. 10. The AlSi10Mg couplers achieve close to 20-dB coupling ( $|S_{31}|$ ) but the transmission coefficient  $|S_{21}|$  is far below desired and the response is not flat. The MCP coupler has less loss than the other components and a mostly flat response; however, the coupling factor is not as designed. The MS coupler performs best; the 20-dB coupling is extremely flat across-band and the observed  $|S_{21}|$  is expected due to the material conductivity. The A3 AlSi10Mg coupler has physically blocked innards due to printing issues. As

TABLE V  
S-PARAMETER DATA FOR WR-10 AND WR-15 AT CENTER FREQUENCIES

Band	Material	$ S_{21} $ (dB)	$ S_{11} $ (dB)
WR-10	Cu	-1.22	-14.87
WR-10	AlSi10Mg A1	-2.01	-14.84
WR-10	AlSi10Mg A2	-1.64	-22.37
WR-10	AlSi10Mg A3	-0.90	-17.91
WR-10	MS	-3.88	-20.50
WR-10	Ni	-3.59	-37.03
WR-10	MCP	-0.57	-24.87
WR-15	AlSi10Mg	-1.58	-31.53
WR-15	MS	-1.21	-21.29

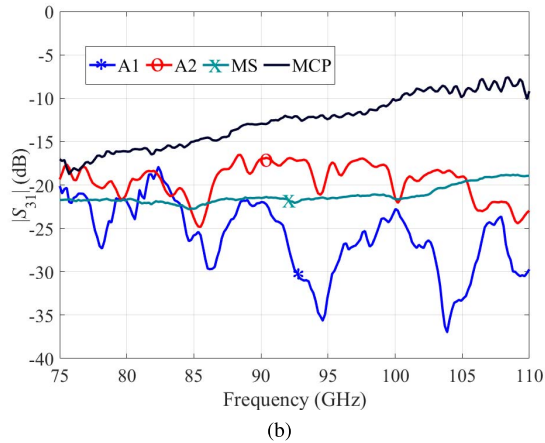
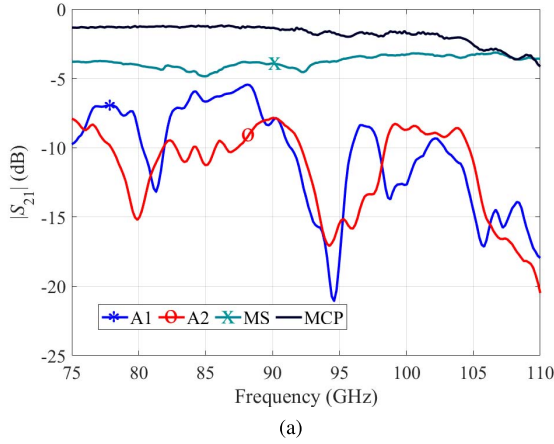


Fig. 10. (a)  $|S_{21}|$  and (b)  $|S_{31}|$  data for the various WR-10 20-dB couplers.

such, the A3 AlSi10Mg sample has no through transmission ( $|S_{21}| \ll 0$  dB) and is excluded in Fig. 10.  $|S_{11}|$  is  $< -10$  dB on average for all components, with  $|S_{11}| < -20$  dB for the MS coupler and isolation  $|S_{41}| < -20$  dB on average for all components.

The  $S$ -parameters of both WR-15 20-dB couplers are shown in Fig. 11. The MS coupler performs best; the response is extremely flat across-band in both  $|S_{21}|$  and  $|S_{31}|$  and matches closely the simulated MS data.

The printing issues in this production run also plagued the AlSi10Mg coupler. Unlike the straight section, the complexity of the coupler does not allow for a thorough cleaning. On average,  $|S_{11}|$  is  $< -20$  dB for both WR-15 components and

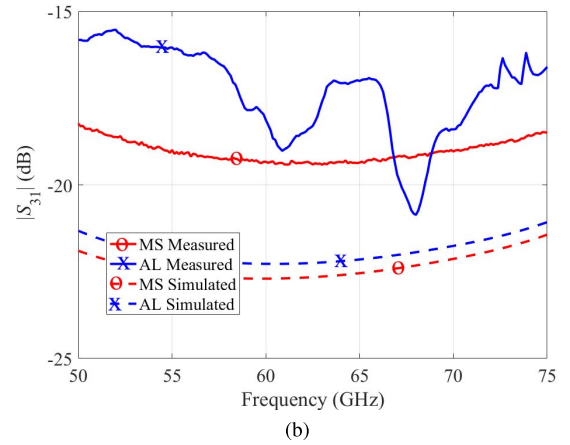
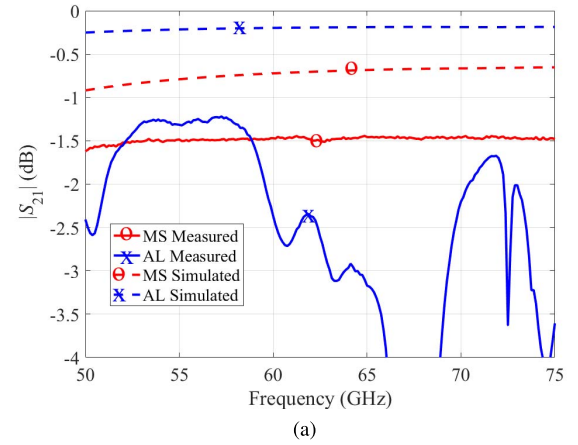


Fig. 11. (a)  $|S_{21}|$  and (b)  $|S_{31}|$  data for the various WR-15 20-dB couplers.  $S$ -parameter data from simulated couplers using the measured 4-point conductivity is also shown.

$|S_{41}|$  is  $< -30$  dB on average for both components with the WR-15 MS coupler  $|S_{41}|$  consistently below  $-40$  dB.

The WR-15 filter sections are designed to have a passband from around 61-65 GHz. In Fig. 12, the simulated filter's  $|S_{21}|$ , using a perfect electric conductor, is shown in black and the  $|S_{21}|$  and  $|S_{11}|$  data of the MS and AlSi10Mg are shown in red and blue, respectively. The null around 64 GHz in the MS could be attributed to liquid expulsion or misprints in corrugation edges.

In comparison to the simulation, the passbands of the printed components are shifted. The shift on AlSi10Mg is more significant than the MS filter. Notice here that the through transmission,  $|S_{21}|$ , of the AlSi10Mg passband is close to, if not less than, the MS  $|S_{21}|$ . Solely based on conductive loss, the aluminum alloy's  $|S_{21}|$  should be about 1 dB less than the MS. However, inconsistent printing issues in the whole aluminum piece cause these shifts and degradation in RF performance.

The loaded and unloaded quality factor,  $Q_L$  and  $Q_U$ , are found using

$$Q_L(f_0) = \frac{f_0}{\Delta f} = Q_U(f_0) * (1 - |S_{21}(f_0)|) \quad (1)$$

where  $\Delta f$  is the 3-dB bandwidth and  $f_0$  is the center frequency [4]. A summary of the loaded and unloaded quality

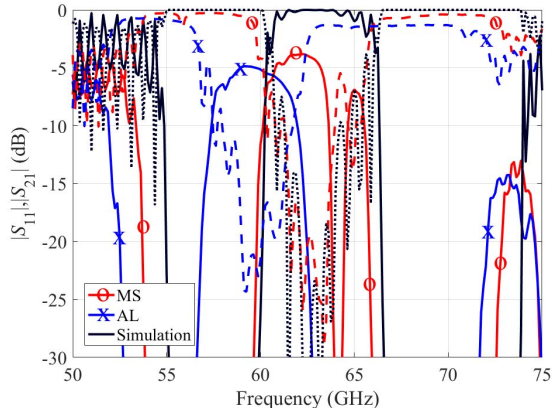


Fig. 12.  $|S_{21}|$  (solid line) and  $|S_{11}|$  (dashed line) data of the WR-15 filter waveguide components. The simulated filter  $|S_{21}|$  data using a perfect electric conductor is shown in black.

TABLE VI  
WR-15 FILTER  $Q$ , LOADED AND UNLOADED

	$Q_L$	$Q_U$
AlSi10Mg	14.03	32.29
MS	19.34	53.50
Ideal	11.62	199.58

factors from printed and simulated WR-15 filters is contained in Table VI. The ideal  $Q$  is for a perfect electric conductor.

#### IV. SURFACE ROUGHNESS ANALYSIS AND RESULTS

Surface roughness and realizable fabrication resolution are the primary limitations in AM millimeter-wave waveguide assemblies [16], [17]. Fabrication feature resolution was discussed in Section II-B; this section focuses on surface roughness characterization. In [18], the spatial bandwidth limitations of FVM, an optical surface finish measurement technique, are analyzed and a measurement protocol is introduced to greatly reduce errors in the technique. The technique described in [18] is used in this paper to characterize the surface finish of the AM waveguide components.

Shown in Fig. 13 are the FVM composite photographs of the waveguide interior surfaces taken during an FVM measurement. Fig. 14 shows the measured deviation in height of the interior of the WR-10 Cu (GRCop-84), WR-10 A3 AlSi10Mg, WR-15 AlSi10Mg, and WR-15 MS waveguides. The RMS surface roughness  $S_q$  and autocorrelation length  $S_{al}$  are typically used to characterize the roughness of machined surfaces. The  $S_q$  value is a measure of the mean deviation of the height and the  $S_{al}$  value gives an idea of how the deviation is distributed laterally.

In this paper, common surface roughness measurement assumptions are made. First, the surface's autocovariance function (ACV) is isotropic and exponential and is modeled as

$$ACV(\tau_x, \tau_y) = (S_q)^2 e^{-\tau/S_{al}} \quad (2)$$

where  $S_q$  is the RMS height variation and  $\tau$  is the lag or displacement. The lag  $\tau$  is defined as  $\tau = (\tau_x^2 + \tau_y^2)^{1/2}$  where  $\tau_x$  and  $\tau_y$  are the 1-D lag in the respective  $x$ - and  $y$ -directions.

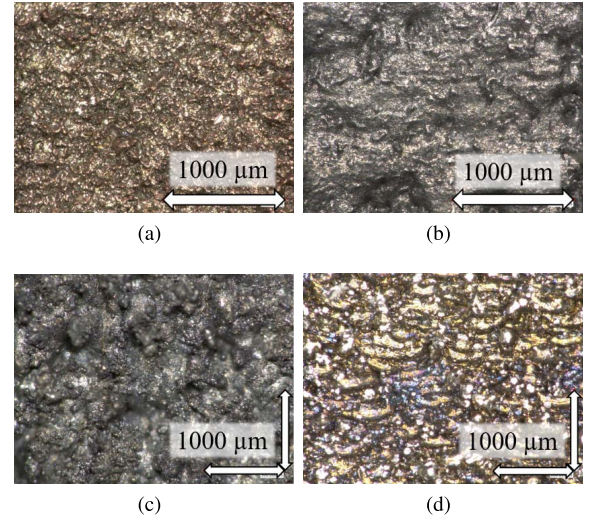


Fig. 13. Composite images of straight waveguide section interior surfaces at  $\times 200$  magnification. (a) WR-10 GRCop-84. (b) WR-10 AlSi10Mg A3. (c) WR-15 AlSi10Mg. (d) WR-15 MS.

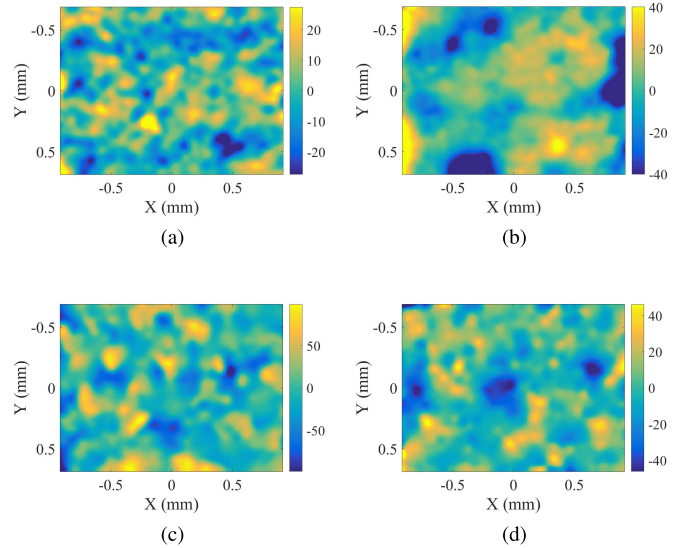


Fig. 14. Measured straight waveguide sections topographical map with colormapped height deviation in  $\mu\text{m}$ . (a) WR-10 GRCop-84. (b) WR-10 AlSi10Mg A3. (c) WR-15 AlSi10Mg. (d) WR-15 MS.

The second assumption is that all height variations,  $S_q$ , follow a Gaussian distribution. Fig. 15 shows the measured comparison to these assumptions for WR-10 GRCop-84. Fig. 15(a) shows an isotropic surface as the lag is homogeneous in the  $x$ - and  $y$ -directions. Fig. 15(b) shows that the normalized surface height variation closely follows a Gaussian distribution. Because the protocol used in the FVM measurements depends on these assumptions to produce accurate results, it is useful to plot the normalized autocorrelation of the measured surface roughness profile, as in Fig. 16.

With the isotropic and exponential behavior of the surface roughness of the fabricated waveguide confirmed, the autocorrelation or autocovariance and RMS surface roughness can accurately be measured. Table VII shows the RMS height, autocorrelation length, and measured loss,  $\alpha_m$ , for the various fabricated components. Surface roughness testing for the Ni

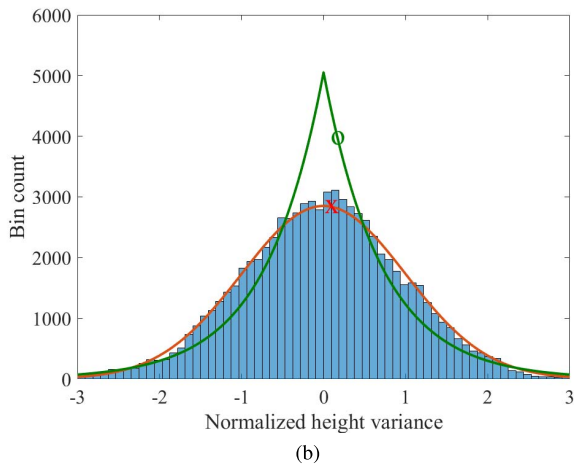
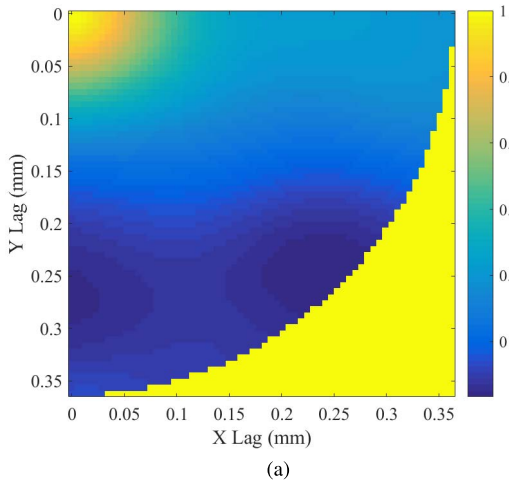


Fig. 15. (a) 2-D array of calculated normalized autocorrelation as a function of  $\tau$  (lag) in  $x$ - and  $y$ -directions from 0 to field-of-view (FOV) divided by  $2\pi$ . (b) Histogram of normalized height variation with Gaussian (X-marker) and exponential (O-marker) curves. Both images use topographical data of the WR-10 GRCop-84 straight waveguide section interior surface at  $\times 200$  magnification for computation.

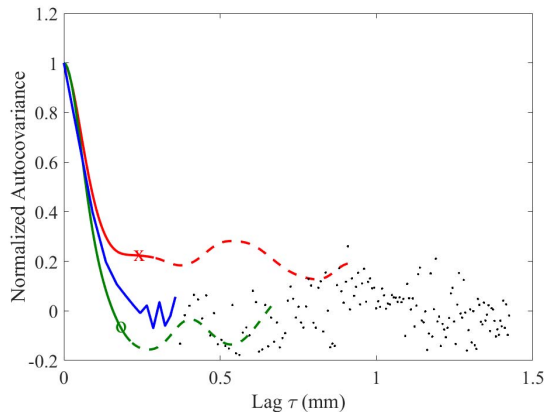


Fig. 16. 1-D computed normalized autocorrelation  $S_q$  (smooth line), for GRCop-84 from the image in Fig. 13(a). Autocorrelation lengths in the horizontal (X-marker) and vertical (O-marker) directions show that computed  $S_q$  is a good fit to the ACV model before edge effects in the FOV limit affect accuracy.

alloy, Inconel 625, was not performed because the material is an extremely durable superalloy and successful destructive testing was not possible.

TABLE VII  
SUMMARY OF AM WAVEGUIDE SURFACE FINISH CHARACTERISTICS AT CENTER FREQUENCIES (92.5 AND 62.5 GHz)

Fab.	Band	Material	$S_q$ ( $\mu\text{m}$ )	$S_{al}$ ( $\mu\text{m}$ )	$\alpha_m$ (dB/m)
3D Printed	W	AlSi10Mg A1	34.95	39.18	22.7
	W	AlSi10Mg A2	31.70	32.19	16.2
	W	AlSi10Mg A3	14.06	144.26	10.3
	W	MS	9.45	42.4	38.8
	W	GRCop-84	12.50	60.85	14.1
	W	Inconel 625	-	-	36.9
	W	Cu MCP	9.46	199.89	5.5
3D Printed	V	AlSi10Mg*	34.95	99.54	11.0
	V	MS	18.14	88.52	14.4
Machined	W	Silver**	-	-	3.54
	V	Silver**	-	-	1.97

\* Using measurement after non-abrasive cleaning.

\*\* Parts ST10R (W-band) and ST15R (V-band) from Custom Microwave, made using Coin Silver (90% Silver, 10% Copper)

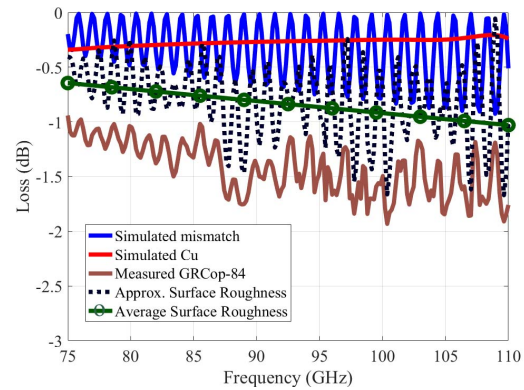


Fig. 17. Different loss mechanisms for GRCop-84 AM waveguide. The surface roughness loss is approximated by subtracting simulated losses (mismatch from aperture dimension deviations and idealized Cu loss) from the measured  $S$ -parameter data. Average surface roughness loss (O-markers) is the moving average of the calculated approximate surface roughness loss.

## V. ANALYSIS

From a loss budget study, it is found that standard models do not accurately predict loss due to surface roughness for surfaces where the RMS height  $S_q$  is much larger than skin depth  $\delta$ . In [19], a commonly used approximation for determining loss due to surface roughness takes the form

$$C_{\text{SR}} = 1 + \frac{2}{\pi} \arctan \left( 1.4 \left( \frac{\sigma}{\delta} \right)^2 \right) \quad (3)$$

where  $C_{\text{SR}}$  is a correction factor applied to the attenuation constant as:  $\alpha_{\text{rough}} = \alpha_{\text{smooth}} C_{\text{SR}}$ . It is seen that the predicted loss saturates at  $2\alpha_{\text{smooth}}$  for WR-10 and WR-15 frequency ranges regardless of material. From the measured loss in Table VII, the WR-10 waveguide components shows the loss near  $4\alpha_{\text{smooth}}$  (using  $\delta_{\text{Cu}} = 0.215 \mu\text{m}$  at 92.5 GHz,  $\sigma_{\text{Cu}} = 4.17 \times 10^{-7} \text{ S/m}$ ), much higher than the predicted  $2\alpha_{\text{smooth}}$ . The WR-10 GRCop-84 waveguide aperture in Fig. 7(a) does not meet the standard WR-10 dimensions resulting in a standing wave in Fig. 17. The approximate surface roughness loss for GRCop-84 waveguide is calculated by subtracting the

mismatch loss and conductor loss due to copper, from the measured  $|S_{21}|$ .

In addition, the measured data from WR-15 components does not agree with (3). In Fig. 9 and for MS, the  $\alpha_{\text{smooth}}$  at 62.5 GHz using measured conductivity is 8.0 dB/m where  $\alpha_m$  is 14.4 dB/m. With the still saturated correction factor (using  $\delta_{\text{MS}} = 1.406 \mu\text{m}$  at 62.5 GHz,  $\sigma_{\text{MS}} = 2.05 \times 10^6 \text{ S/m}$ ), the predicted surface roughness is larger than measured; here, the  $\alpha_m$  is equal to  $1.8\alpha_{\text{smooth}}$ . Equation 3 is most common in commercial electromagnetic simulators, but the conclusion from the measurements in this paper is that it does not accurately predict loss at V- and W-bands for very rough surfaces ( $S_q \gg \delta$ ).

## VI. CONCLUSION

This paper presents several V-band (50–75 GHz) WR-15 and W-band (75–110 GHz) WR-10 waveguide components fabricated using mainly DMLS in aluminum, nickel-chromium, MS, and copper alloys. Printing resolution is analyzed with respect to feature creation, RF performance is measured, and surface roughness and the respective loss are quantified. The measured loss for WR-10 waveguide parts at 92.5 GHz ranges from 5.5 dB/m for the copper-plated plastic waveguides to 36.9 dB/m for the nickel alloy. For WR-15 components at 62.5 GHz, the loss ranges from 11.0 dB/m for the aluminum alloy to 14.4 dB/m for the MS alloy.

With current available technologies, the experimental data indicates as follows.

- 1) Copper (GRCop-84) is too soft to work with reliably and prints nonprecise dimensions.
- 2) Nickel (Inconel 625) is extremely durable, but loss is high.
- 3) SLA (and other plated-plastics) is too fragile in demanding environments, but has low loss.
- 4) Aluminum (AlSi10Mg) has issues of printing repeatability and feature resolution.
- 5) MS performs best in printing features but has higher loss.

We suggest that MS appears to be a good candidate for metal waveguide printing given precision, structural integrity, and reasonable conductivity. MS with possible additional electroplating holds the promise for inexpensive DMLS millimeter-wave waveguide components with high performance.

## ACKNOWLEDGMENT

The authors would like to thank B. Wallace at DARPA for helpful discussions. The authors would also like to thank colleagues at Midwest Composite, Visser Precision, and Protolabs for useful information and direction in the component build process.

## REFERENCES

[1] J. R. Montejó-Garai, I. O. Saracho-Pantoja, C. A. Leal-Sevillano, J. A. Ruiz-Cruz, and J. M. Rebollar, "Design of microwave waveguide devices for space and ground application implemented by additive manufacturing," in *Proc. Int. Conf. Electromagn. Adv. Appl.*, Turin, Italy, Sep. 2015, pp. 325–328.

[2] J. Thornton, B. Dalay, and D. Smith, "Additive manufacturing of waveguide for Ku-band satellite communications antenna," in *Proc. 10th Eur. Conf. Antennas Propag. (EuCAP)*, Davos, Switzerland, 2016, pp. 1–4.

[3] A. I. Dimitriadis, M. Favre, M. Billod, J.-P. Ansermet, and E. de Rijk, "Design and fabrication of a lightweight additive-manufactured Ka-band horn antenna array," in *Proc. 10th Eur. Conf. Antennas Propag. (EuCAP)*, Davos, Switzerland, 2016, pp. 1–4.

[4] M. D'Auria *et al.*, "3-D printed metal-pipe rectangular waveguides," *IEEE Trans. Compon., Packag., Manuf. Technol.*, vol. 5, no. 9, pp. 1339–1349, Sep. 2015.

[5] A. Tamayo-Domínguez, J.-M. Fernández-González, and M. Sierra-Pérez, "Groove gap waveguide in 3-D printed technology for low loss, weight, and cost distribution networks," *IEEE Trans. Microw. Theory Techn.*, vol. 65, no. 11, pp. 4138–4147, Nov. 2017.

[6] Y. Arbaoui *et al.*, "Full 3-D printed microwave termination: A simple and low-cost solution," *IEEE Trans. Microw. Theory Techn.*, vol. 64, no. 1, pp. 271–278, Jan. 2016.

[7] X. Shang *et al.*, "W-band waveguide filters fabricated by laser micromachining and 3-D printing," *IEEE Trans. Microw. Theory Techn.*, vol. 64, no. 8, pp. 2572–2580, Aug. 2016.

[8] B. Zhang and H. Zirath, "3D printed iris bandpass filters for millimeter-wave applications," *Electron. Lett.*, vol. 51, no. 22, pp. 1791–1793, Oct. 2015.

[9] B. Zhang and H. Zirath, "Metallic 3-D printed rectangular waveguides for millimeter-wave applications," *IEEE Trans. Compon., Packag., Manuf. Technol.*, vol. 6, no. 5, pp. 796–804, May 2016.

[10] M. Coffey, S. Verploegh, S. Edstaller, S. Armstrong, E. Grossman, and Z. Popovic, "Additive manufactured W-band waveguide components," in *IEEE MTT-S Int. Microw. Symp. Dig.*, Honolulu, HI, USA, Jun. 2017, pp. 52–55.

[11] P. Uliasz, T. Knych, M. Piwowarska, and J. Wiecheć, "The influence of heat treatment parameters on the electrical conductivity of AlSi7Mg and AlSi10Mg aluminum cast alloys," in *ICAA13 Pittsburgh*. Cham, Switzerland: Springer, 2012.

[12] D. L. Ellis, D. J. Keller, and M. Nathal, "Thermophysical properties of GRCop-84," NASA GRC, Cleveland, OH, USA, Tech. Rep. NASA/CR-2000-210055, Jun. 2000.

[13] C. A. Basca, M. Talos, and R. Brad, "Randomized hough transform for ellipse detection with result clustering," in *Proc. Int. Conf. Comput. Tool (EUROCON)*, Belgrade, Serbia, 2005, pp. 1397–1400.

[14] Y. Xie and Q. Ji, "A new efficient ellipse detection method," in *Proc. 16th Int. Conf. Pattern Recognit.*, vol. 2, 2002, pp. 957–960.

[15] X. He, J. T. Norris, P. W. Fuerschbach, and T. DebRoy, "Liquid metal expulsion during laser spot welding of 304 stainless steel," *J. Phys. D, Appl. Phys.*, vol. 39, no. 3, p. 525, 2006.

[16] B. Zhang *et al.*, "Metallic 3-D printed antennas for millimeter- and submillimeter wave applications," *IEEE Trans. THz Sci. Technol.*, vol. 6, no. 4, pp. 592–600, Jul. 2016.

[17] A. Townsend, N. Senin, L. Blunt, R. K. Leach, and J. S. Taylor, "Surface texture metrology for metal additive manufacturing: A review," *Precis. Eng.*, vol. 46, pp. 34–47, Oct. 2016.

[18] E. N. Grossman, M. Gould, and N. P. Mujica-Schwann, "Robust evaluation of statistical surface topography parameters using focus-variation microscopy," *Surf. Topogr. Metrol. Properties*, vol. 4, no. 3, p. 035003, Sep. 2016.

[19] E. Hammerstad and O. Jensen, "Accurate models for microstrip computer-aided design," in *IEEE MTT-S Int. Microw. Symp. Dig.*, Washington, DC, USA, 1980, pp. 407–409.



**Shane Verploegh** (M'14) received the B.S. degree in electrical engineering from the University of Notre Dame, Notre Dame, IN, USA, in 2014. He is currently pursuing the Ph.D. degree in electrical engineering at the University of Colorado, Boulder, CO, USA.

From 2014 to 2016, he was a Nuclear Power Instrumentation and Controls Associate with Sargent & Lundy, Chicago, IL, USA. His current research interests include additive manufacturing for millimeter-wave applications and efficient high-power monolithic microwave integrated circuit power amplifier design.



**Mike Coffey** (M'10) received the B.S. degree in electrical engineering from California State Polytechnic University, Pomona, CA, USA, in 2010, and the M.S. and Ph.D. degrees in electrical engineering from the University of Colorado, Boulder, CO, USA, in 2014 and 2017, respectively.

From 2010 to 2012, he was with the Advanced Technology Department, Wavestream Corporation, where he was involved in high power X–Ka-band satellite transmitters and transceivers for military and civilian applications. He is currently with Mission Microwave Technologies, Los Angeles, CA, USA, where he is in charge of monolithic microwave integrated circuit (MMIC) development for SATCOM applications. His current research interests include MMIC power amplifier design, efficient and linear amplifier architectures, wireless power transfer, and nonlinear stability analysis techniques.



**Erich Grossman** (M'88–SM'06) received the A.B. degree in physics from Harvard College, Harvard University, Cambridge, MA, USA, in 1980, and the Ph.D. degree in physics from the California Institute of Technology, Pasadena, CA, USA, in 1987.

From 1988 to 1989, he was a Post-Doctoral Fellow with The University of Texas at Austin, Austin, TX, USA. In 1989, he joined the National Institute of Standards and Technology (NIST), Boulder, CO, USA, where he is currently a Physicist with the Physical Measurement Laboratory, involved in infrared and submillimeter system development. His notable accomplishments include the demonstration of the world's highest frequency high-efficiency lithographic antennas, the world's highest frequency Josephson junctions (awarded a Department of Commerce Gold Medal in 1993), and conception and early development of the SQUID multiplexer. More recently, he has developed several 0.11 THz cameras for security applications.

Dr. Grossman was a recipient of the Allen V. Astin Measurement Science Award in 2010.



**Zoya Popović** (S'86–M'90–SM'99–F'02) received the Dipl.Ing. degree from the University of Belgrade, Belgrade, Serbia, and the Ph.D. degree from the California Institute of Technology, Pasadena, CA, USA.

From 2001 to 2003, she was a Visiting Professor with the Technical University of Munich, Munich, Germany, and a Visiting Professor with the Institut Supérieur de l'Aéronautique et de l'Espace, Toulouse, France, in 2014. She is currently a Distinguished Professor and the Lockheed Martin Endowed Chair of electrical engineering with the University of Colorado, Boulder, CO, USA. She has graduated 56 Ph.D. students and currently advises 12 doctoral students. Her current research interests include high-efficiency power amplifiers and transmitters, microwave and millimeter-wave high-performance circuits for communications and radar, medical applications of microwaves, millimeter-wave and terahertz quasi-optical techniques, and wireless powering.

Prof. Popovic was a recipient of two IEEE MTT-S Microwave Prizes for best journal papers, the White House NSF Presidential Faculty Fellow Award, the URSI Issac Koga Gold Medal, the ASEE/HP Terman Medal, and the German Humboldt Research Award. She was elected as Foreign Member of the Serbian Academy of Sciences and Arts in 2006. She was named the IEEE MTT-S Distinguished Educator in 2013 and the University of Colorado Distinguished Research Lecturer in 2015.